



MAPPING DRYING SHRINKAGE DEFORMATIONS IN CEMENT-BASED MATERIALS

C.M. Neubauer,* H.M. Jennings,^{1*}† and E.J. Garboczi‡

*Department of Materials Science and †Department of Civil Engineering, Northwestern University, Evanston, IL 60208

‡National Institute of Standards and Technology, Gaithersburg, MD 20899

(Refereed)

(Received February 10, 1997; in final form October 14, 1997)

ABSTRACT

A new technique for mapping the deformations in a digital image of microstructure is presented. This technique works on any set of two digital images of the same area taken before and after deformations are generated. Results for cement paste show that the deformations are distributed as large compactions separated by crack-like rarefactions. The rarefactions may represent the precursor to microcracking. The results suggest that macro-scale deformation is the result of a competition between expanding and contracting parts of the matrix. Individual microdeformations can then be much higher in magnitude than average macrodeformations. A single shrinkage value like the average macrodeformation does not, therefore, adequately represent the microstructural processes occurring during drying shrinkage. © 1997 Elsevier Science Ltd

Introduction

One of the major causes of failure in cement-based materials is drying shrinkage, the deformation associated with loss of water. Degradation due to drying shrinkage can occur both directly through drying shrinkage cracking, which introduces flaws into the matrix of the material, or indirectly through secondary reactions, which occur as reactive ions diffuse rapidly into the material via the crack pathways. Four basic mechanisms, which are functions of relative humidity (RH), are thought to control drying shrinkage in cement-based materials:

- 1) Capillary stress (100%–40% RH) is due to the menisci of water in the partially filled capillary pores transferring tension to the pore walls, causing contraction and shrinkage (1–6).
- 2) Disjoining pressure (100%–40% RH) is caused by adsorbed water evaporating from the surfaces of adjoining C-S-H particles, resulting in shrinkage as the water layer becomes thinner (1–4).

¹To whom correspondence should be addressed.

- 3) Gibbs-Bangham shrinkage ($<40\%$ RH) is due to an increase in C-S-H specific surface free energy as adsorbed surface water is removed, causing shrinkage as the material tries to reduce its surface area (1–6).
- 4) Loss of the final monolayer of interlayer water ($<11\%$ RH), which occurs within the layers of an individual C-S-H particle as the final layer of adsorbed water is removed (1–6).

Of these mechanisms, disjoining pressure is often considered to be of the least importance. It causes only very small deformations, much smaller than those measured in this paper. Thus, for the purposes of this paper, disjoining pressure can be considered insignificant.

A major difficulty in studying drying shrinkage is distinguishing between *real* mechanisms and *apparent* mechanisms (7). Real mechanisms are the result of the material properties and are independent of specimen geometry, while apparent mechanisms are strongly dependent on specimen geometry and are the result of moisture gradients that occur during the drying process. In order to study real mechanisms, which are usually masked by apparent mechanisms, very small or thin samples are typically used.

In order to investigate the real mechanisms controlling drying shrinkage in cement-based materials, a recent study used an environmental scanning electron microscope (ESEM) to study drying shrinkage on the micrometer level (8,9). Samples were placed in the chamber of the ESEM, and a series of images was taken at increments of relative humidities between 90% and 5%, where the 90% RH image was taken as the zero displacement base. An image intensity matching technique (IIMT) was developed and used to compare the digital images to the 90% RH base and determine displacements between them. Displacements can be determined with the IIMT to a resolution of ± 0.2 pixels (10). Using these displacements, an average value for shrinkage across the field of view was calculated. However, not enough information was acquired to determine the physical distribution of deformations. In composite materials such as cement systems, strain concentrations at internal interfaces may dominate behavior, so that the physical distribution of deformations provides more valuable information than does a single number.

It is important to differentiate between deformation and elastic strain to provide a clear understanding of the following analysis. Deformation is analogous to elastic strain as both can be defined as the change in length over the initial length. However, elastic strain, either in the linear limit of small strains (11), or in the more general finite strain regime (12,13), implies that the stress state can be determined by simply multiplying by the appropriate modulus. However, drying shrinkage is a highly inelastic situation, with a large visco-elastic component. Debonding can occur and rearrangement of phases is possible, which can result in unusually large local displacements. Thus, while the deformations within the microstructure are computed from the displacements using a finite strain formulation, they cannot be related directly to a stress state as in the finite strain elastic case (12,13). Therefore, deformation is a more accurate term to describe the analysis presented in this paper. Throughout the rest of this paper, the term *rarefaction* will be used to describe features that increase in size (analogous to undergoing a tensile strain), and the term *compaction* will be used to describe features that decrease in size (analogous to undergoing a compressive strain).

This paper gives a brief description of a new deformation mapping technique (DMT) that does provide information on the physical distribution of deformations throughout the microstructure. More complete descriptions of both the IIMT and DMT techniques can be found

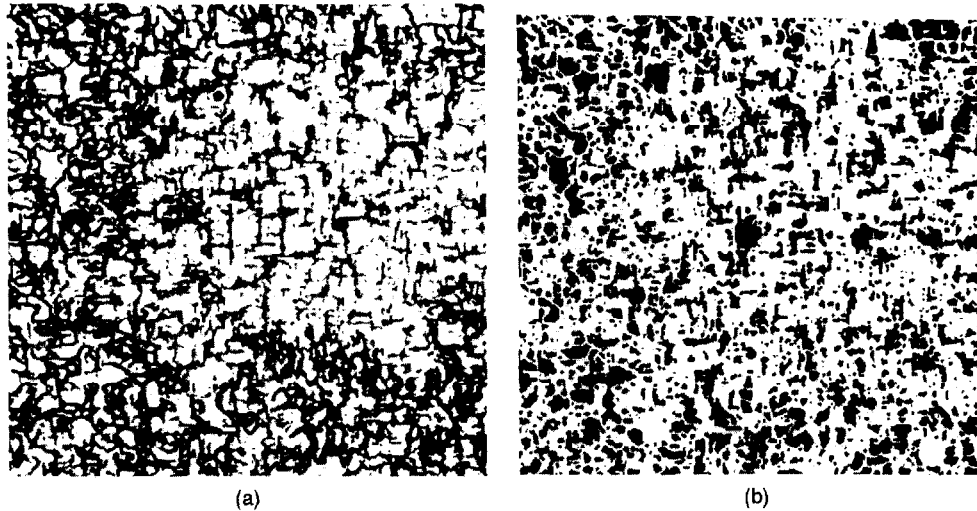


FIG. 1.

Deformation maps achieved upon drying from 90% RH to 50% RH for 4-day-old ordinary Portland cement samples with $w/c = 0.3$: *a*) rarefactions, and *b*) compactions. Field of view = 97 μm . Darker colors indicate higher deformation levels.

elsewhere (14). Preliminary results are presented and compared with the previous drying shrinkage study (8,9).

Description of the Deformation Mapping Technique

The IIMT and DMT require two digital images, one taken before the deformations develop (the *reference image*) and one taken after the deformations develop in the microstructure (the *deformed image*). The source of the deformations is irrelevant, with the most likely sources being mechanical, thermal, or environmental sources. Each image is stored digitally as an array of gray scales where the number 255 represents white and the number 0 represents black. These two images must be taken under the same magnification or the analysis becomes invalid.

The vector displacement of each pixel is then calculated using the IIMT. This technique is described in detail elsewhere (10). In simple terms, it finds the displacements of the deformed image that represents the minimum of the difference in intensity between this image and the reference image.

Using the displacement field generated by the IIMT, it becomes possible to evaluate the deformations in the image through the general deformation tensor (which is mathematically equivalent to the strain tensor). The deformation tensor at a given point is defined by (11):

$$\Phi_{ik} = \frac{1}{2} \left(\frac{\partial u_i}{\partial x_k} + \frac{\partial u_k}{\partial x_i} + \frac{\partial u_i}{\partial x_l} \frac{\partial u_l}{\partial x_k} \right) \quad i, k, l = 1, 2 \quad (1)$$

where Φ_{ik} is the deformation tensor, u_i is the i th component of the displacement vector at the given point, and x_k is the Cartesian variable in the k th direction. This is the

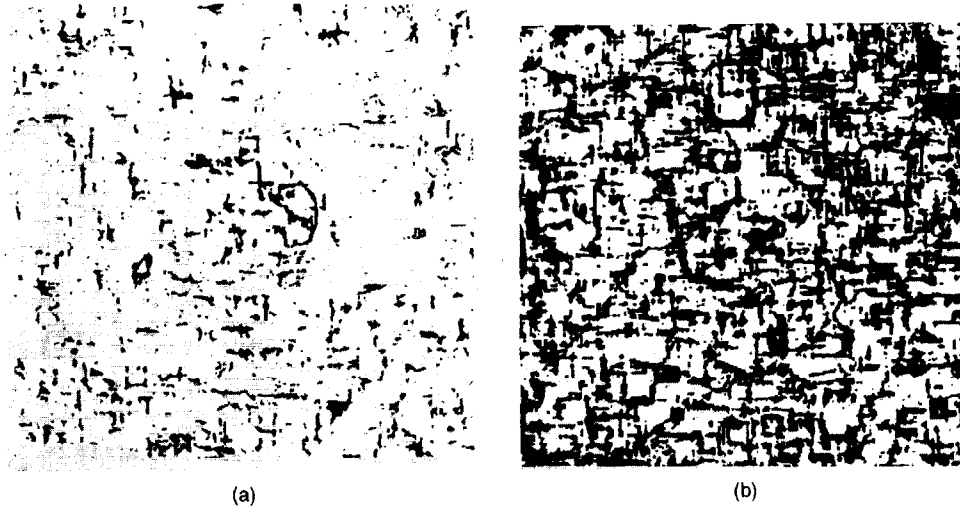


FIG. 2.

Deformation maps achieved upon drying from 90% RH to 50% RH for 28-day-old ordinary Portland cement samples with $w/c = 0.3$: *a*) rarefactions, and *b*) compactions. Field of view = 97 μm . Darker colors indicate higher deformation levels.

complete deformation tensor, and does not use the linear approximation for small deformations. We have found that the complete tensor is necessary because local deformations in a microstructure can be large, well beyond the small displacement limit, especially when cracking or debonding occurs. The three independent elements (ϕ_{11} , ϕ_{22} , and ϕ_{12}) of the deformation tensor are calculated, and averaged over a pixel. From these elements the principal deformations are determined by diagonalizing the deformation tensor:

$$\phi_{11}^*, \phi_{22}^* = \frac{(\phi_{11} + \phi_{22}) \pm \sqrt{[(\phi_{11} + \phi_{22})^2 - 4(\phi_{11}\phi_{22} - \phi_{12}^2)]}}{2} \quad (2)$$

where ϕ_{11}^* and ϕ_{22}^* are the average principal deformations of the given pixel. These values can then be used to calculate the average linear deformation in each pixel through Eq. 3:

$$\phi = \frac{\Delta l}{l} = \frac{\sqrt{(1 + \phi_{11}^*)(1 + \phi_{22}^*)} - 1}{1} \quad (3)$$

When ϕ_{11}^* and ϕ_{22}^* are small, Eq. 3 reduces to a simple arithmetic mean. The local average linear deformation is then mapped across the microstructure to provide a physical representation of its distribution in the sample. Additionally, the average linear deformation in each pixel can be counted and represented as a histogram, or deformation distribution. Examples of these distributions are presented below. This definition of the local deformation does not assume that the material is elastic, but is simply a measure of the geometric deformation due to recoverable and unrecoverable elastic and viscoelastic processes.

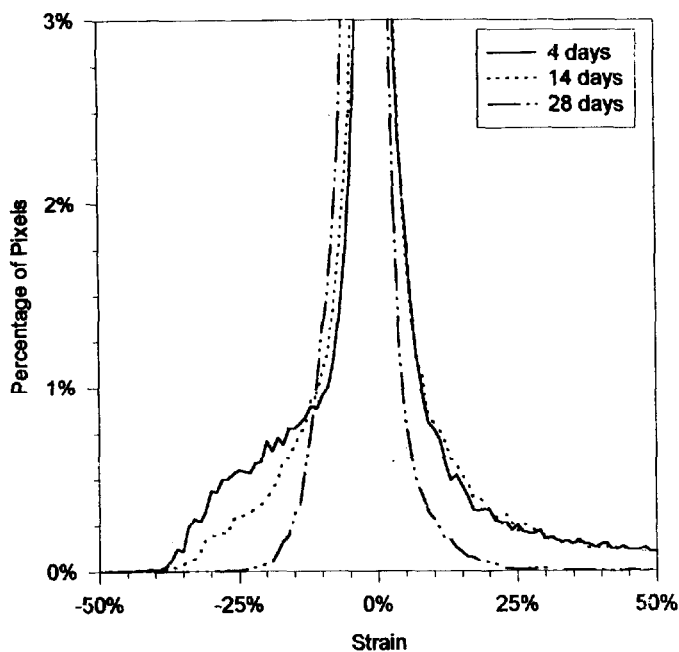


FIG. 3.

Deformation distribution achieved upon drying from 90% RH to 50% RH for 4-, 14-, and 28-day-old samples with $w/c = 0.3$.

Preliminary Results

Experimental Procedure

Images were acquired using an environmental scanning electron microscope (ESEM). The samples were made from fracture surfaces that were approximately 100 mm^2 in area and 1 mm thick. Whenever possible, a relatively smooth region of the fracture surface was chosen to eliminate surface irregularities that diminish the performance of the IIMT. Each sample was attached to a sample stub with a light glue coating, placed in the specimen chamber at 90% RH, and allowed to equilibrate for approximately 30 min. Images of selected areas were then taken. The relative humidity was then dropped to 50% RH and again allowed to equilibrate for approximately 30 min. Digital images of the same areas were taken at identical magnifications. This process was repeated at 5% RH. The temperature was held constant at 10°C throughout, and changes in relative humidity were induced by changing the water vapor pressure in the specimen chamber. Each image was 512×512 pixels in size.

Effects of Age

Figures 1 and 2 show the deformation maps produced upon drying from 90% RH to 50% RH for 4- and 28-day-old samples of Portland cement paste mixed at a water/cement (w/c) mass ratio of 0.3. Figures 1a and 2a show the rarefactions, which form areas that extend in only

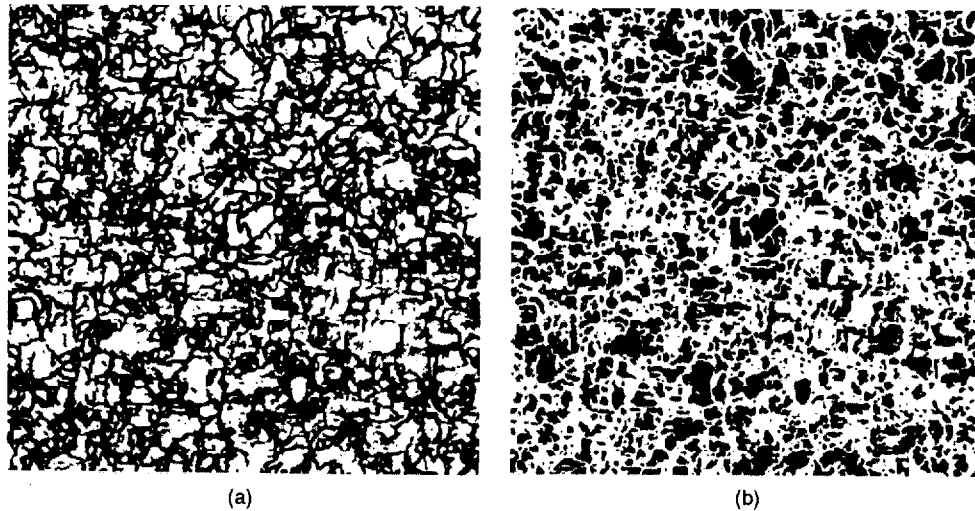


FIG. 4.

Deformation maps achieved upon drying from 90% RH to 5% RH for 4-day-old ordinary Portland cement samples with $w/c = 0.3$: *a*) rarefactions, and *b*) compactions. Field of view = 97 μm . Darker colors indicate higher deformation levels.

one direction, and thus are “crack-like.” Figures 1b and 2b show the compactions, which tend to form areas that are extended in two directions.

Figure 3 shows the deformation distribution functions, $f(\epsilon)$, for 4-, 14-, and 28-day-old samples. The deformation distribution function is defined such that $f(\epsilon)d\epsilon$ is the area fraction of the image (percentage of pixels) that has a deformation lying between ϵ and $\epsilon + d\epsilon$. As was mentioned before, all the images were 512×512 pixels squared, so that all the deformation distribution functions presented have the same normalization, i.e., the same area under the curve. For drying from 90% RH to 50% RH, the 4-day sample has the widest deformation distribution, with the 14-day sample next, and the 28-day sample showing the narrowest deformation distribution. The map for the 14-day-old sample is not shown, but resembles the 4-day-old (Fig. 1) and 28-day-old (Fig. 2) maps. Previous microstructural drying shrinkage studies (8,9) showed that young samples also had a higher *average* shrinkage deformation than did older samples.

Upon drying from 90% RH to 5% RH, much higher deformation levels are attained at all ages, as shown in Figures 4 and 5 for the same material. Figure 4 shows deformation maps for a 4-day-old specimen, which is typical of those produced at other ages. Rarefactions are aligned in a crack-like pattern that branches throughout the sample, while compactions are found in separated fields almost uniformly distributed throughout the sample. These rarefactions may represent a precursor to microcracking as no visible cracks form.

Figure 5 shows the deformation distributions at all three ages, for 90% to 5% RH drying. The high deformation regions are composed of many more pixels than those achieved upon drying from 90% RH to 50% RH, because the deformation distribution functions are much broader and less peaked than those shown in Figure 3.

The three distributions seem qualitatively similar at first sight, but there are differences. The 14- and 28-day samples have a peaked structure near 0% deformation, which is not

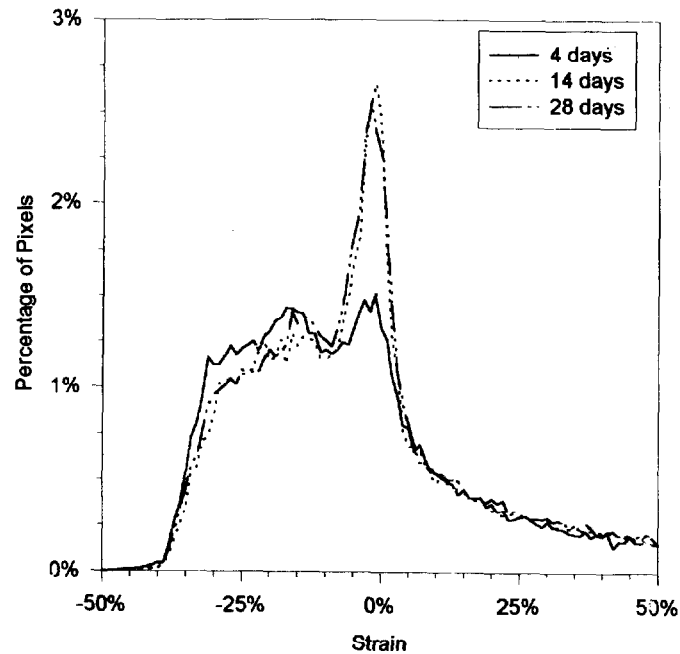


FIG. 5.

Deformation distribution achieved upon drying from 90% RH to 5% RH for 4-, 14-, and 28-day-old samples with $w/c = 0.3$.

shared by the 4-day sample. However, because the total area under the curves must be the same, one can see that at more negative deformations, the 4-day sample distribution is higher than the 14- and 28-day distributions. At positive deformation, the distributions are almost identical. Previous studies (8,9) have found that the average shrinkage deformation of older samples are much less than those for young samples upon drying from 90% to 5% RH, which is generally consistent with the literature. In terms of the deformation distributions, the average deformation is defined as the integral of the deformation weighted by the deformation distribution. The deformation distributions shown in Figure 5 are consistent with this finding, as the higher weight at large magnitude deformations for the 4-day-old samples, and the higher weight at small magnitude deformations for the 14- and 28-day samples, will result in the average deformation of the 4-day sample being negative and larger in magnitude than the 14- and 28-day samples.

One must remember that average shrinkage deformations are around -1% (8,9). The average shrinkage deformation for different age samples range from 0.1 to 1.0%. Compared to the width of the deformation distributions, these are not large differences. There is clearly a complicated competition going on between the expanding and contracting parts of the microstructure, which controls the average shrinkage deformation or overall deformation. For example, one deformation distribution can be broader than another, and yet still have a lower average deformation, depending on how the weight of the distribution is distributed.

A material with low overall deformation could either have many very small deformation regions, or many very high deformation regions with opposing signs, as long as they nearly balance. Similarly, a material with high overall deformation could contain more regions of

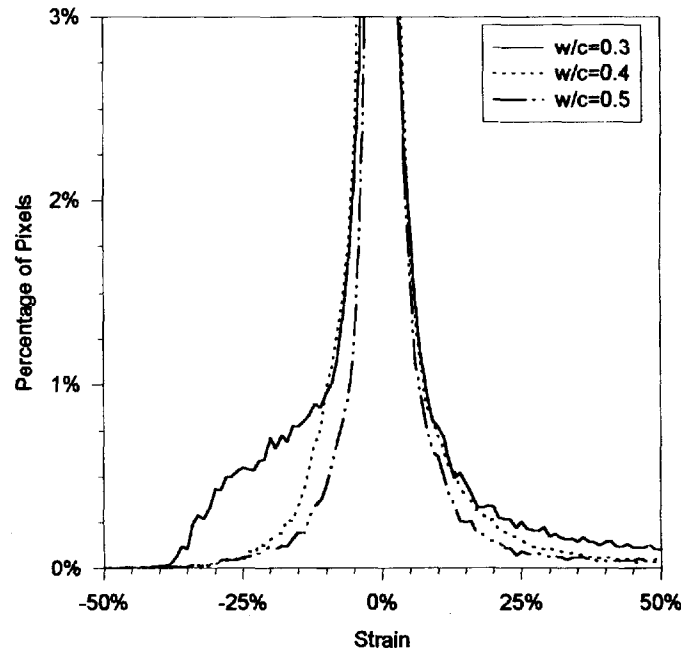


FIG. 6.

Deformation distribution achieved upon drying from 90% RH to 50% RH for 4-day-old samples with $w/c = 0.3, 0.4$, and 0.5 .

small deformation with similar signs, or many regions of large deformations with opposing signs but with a bias in one direction of deformation. Regardless, it is apparent that to represent shrinkage by a single number is an over-simplification.

Effects of w/c

Figures 6 and 7 show the deformation distributions produced upon drying from 90% RH to 50% RH and 90% RH to 5% RH, respectively, for 4-day-old samples of Portland cement mixed at water/cement (w/c) ratios of 0.3, 0.4, and 0.5. In Figure 6, upon drying from 90% RH to 50% RH, the highest level of deformation in the distribution is in the $w/c = 0.3$ sample, which is the broadest deformation distribution. The distributions become less broad as w/c increases. However, the average shrinkage deformation decreases as w/c decreases (8,9). The results for the deformation distributions after drying from 90% RH to 5% RH are shown in Figure 7. All the deformation distributions are qualitatively similar, although the higher w/c samples are known to have a higher average shrinkage deformation (8,9). Just as for the different age samples, the different w/c samples have average shrinkage deformations ranging from 0.1 to 1.0%. These differences among average deformations are small compared to the width of the deformation distributions, so that there only has to be small differences in the deformation distributions in order to achieve these average deformation differences. Again, the competition mentioned above, and the dangers inherent in representing this complicated phenomenon with a single value, are evident.

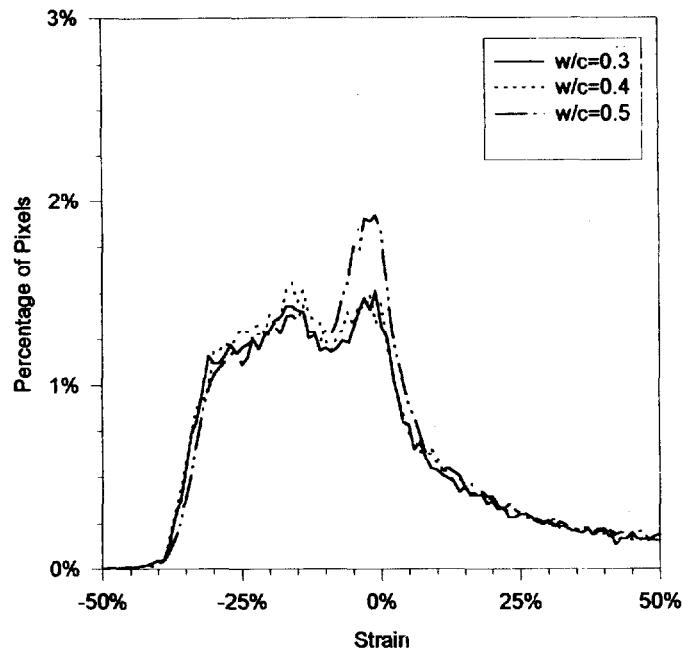


FIG. 7.

Deformation distribution achieved upon drying from 90% RH to 5% RH for 4-day-old samples with $w/c = 0.3, 0.4$, and 0.5 .

Conclusions

A new technique for mapping the deformations in a digital image of microstructure has been presented. This technique will work on any set of two digital images of the same area taken before and after deformations are generated. The deformations can be large, and can come from elastic and visco-elastic processes. Early results show that the deformations are distributed as large compactions separated by crack-like rarefactions. These rarefactions may represent the immediate precursors to microcracking. A broader deformation distribution can have a smaller average deformation, and qualitatively similar distributions can result in different average shrinkage deformations. Thus, a single shrinkage value does not adequately represent the microstructural processes occurring during drying shrinkage. More research is needed before the subtleties of these complicated processes can be understood and possibly controlled.

Acknowledgment

We gratefully acknowledge the financial support provided by the Department of Energy (Award Number DE-FG02-91ER45460/A01). We also wish to thank the National Science Foundation Center for Advanced Cement-Based Materials for providing the facilities used in this study. CMN wishes to thank the Department of Defense for funding through a National Defense Science and Engineering Graduate Fellowship.

References

1. H.F.W. Taylor, *Cement Chemistry*, Academic Press, Inc., London, 1990.
2. S. Mindess and J.F. Young, *Concrete*, Prentice-Hall, Inc., Englewood Cliffs, NJ, 1981.
3. Y. Xi and H.M. Jennings, *Materials Science of Concrete III*, J.P. Skalny (ed.), p. 37, American Ceramic Society, Westerville, OH, 1992.
4. C.F. Ferraris and F.H. Wittmann, *Cem. Concr. Res.* 17, 453 (1987).
5. W. Hansen, *J. Am. Ceram. Soc.* 70, 323 (1987).
6. J.A. Almudaiheem, *J. King Saud Univ., Engng. Sci.* 1, 69 (1991).
7. F.H. Wittmann, *Fundamental Research on Creep and Shrinkage of Concrete*, F.H. Wittmann (ed.), p. 129, Martinus Nijhoff Publishers, Boston, MA, 1982.
8. T.B. Bergstrom, Ph.D. Thesis, Northwestern University, Evanston, IL, 1993.
9. C.M. Neubauer, T.B. Bergstrom, Y. Xi, K. Sujata, E.J. Garboczi, and H.M. Jennings, submitted to *J. Mater. Res.* (1996).
10. Y. Xi, T.B. Bergstrom, and H.M. Jennings, *Comput. Mater. Sci.* 2, 249 (1994).
11. L.D. Landau and E.M. Lifshitz, *Theory of Elasticity*, Pergamon Press, Oxford, 1986.
12. D.C. Wallace, *Phys. Rev.* 162, 776 (1967).
13. R.N. Thurston, *J. Acoust. Soc. Am.* 37, 348 (1965).
14. C.M. Neubauer, H.M. Jennings, and E.J. Garboczi, submitted to *Mater. Struct.* (1997).